

## Article

# Effects of Plasmonic Au Nanoparticles on the Optical Nonlinearity of InAs/GaAs Quantum Dot Semiconductor Saturable Absorber Mirrors

Hongpei Wang <sup>1</sup>, Hao Dai <sup>2</sup>, Menglu Lyu <sup>2</sup>, Cheng Jiang <sup>2,\*</sup>, Shulong Lu <sup>1,\*</sup> and Ziyang Zhang <sup>2</sup>

<sup>1</sup> School of Nano-Tech and Nano-Bionics, University of Science and Technology of China, Hefei 230026, China; hpwang@mail.ustc.edu.cn

<sup>2</sup> College of Electronics and Information, Qingdao University, Qingdao 266071, China; 2021020653@qdu.edu.cn (H.D.); lvmenglu@qdu.edu.cn (M.L.); zyzhang2021@qdu.edu.cn (Z.Z.)

\* Correspondence: cjiang2017@sinano.ac.cn (C.J.); sllu2008@sinano.ac.cn (S.L.)

**Abstract:** Au nanoparticles (NPs) were designed to be embedded into III-V semiconductors to form Au/GaAs Schottky heterostructures, which were used as top-modified cover layers for quantum dot semiconductor saturable absorption mirrors (QD-SESAMs). By harnessing the distinctive localized surface plasmon resonance (LSPR) effect exhibited by Au NPs, a remarkable enhancement in photogenerated carrier concentration is achieved at the heterojunction interface. Consequently, this leads to a significant improvement in the nonlinear optical characteristics of the device. The modulation depth (MD) and saturation fluence of the device are optimized from the initial 2.2% and 16.1 MW/cm<sup>2</sup> to 2.8% and 8.3 MW/cm<sup>2</sup>, respectively. Based on the optimized device, a Q-switched laser has been developed with an impressive output power of 17.61 mW and a single pulse energy of 274.9 nJ. These results unequivocally showcase the exceptional advantages offered by utilizing Au NPs to optimize the nonlinear optical characteristics of III-V semiconductor devices, thereby highlighting its immense potential for practical applications in various fields.

**Keywords:** Au nanoparticles; III-V semiconductors; localized surface plasmon resonance; nonlinear optical characteristics



**Citation:** Wang, H.; Dai, H.; Lyu, M.; Jiang, C.; Lu, S.; Zhang, Z. Effects of Plasmonic Au Nanoparticles on the Optical Nonlinearity of InAs/GaAs Quantum Dot Semiconductor Saturable Absorber Mirrors. *Photonics* **2024**, *11*, 235. <https://doi.org/10.3390/photonics11030235>

Received: 7 February 2024  
Revised: 26 February 2024  
Accepted: 28 February 2024  
Published: 5 March 2024



**Copyright:** © 2024 by the authors. Licensee MDPI, Basel, Switzerland. This article is an open access article distributed under the terms and conditions of the Creative Commons Attribution (CC BY) license (<https://creativecommons.org/licenses/by/4.0/>).

## 1. Introduction

Noble metal nanoparticles (NPs) exhibit pronounced light absorption due to the phenomenon of localized surface plasmon resonance (LSPR) [1], which has garnered significant attention in diverse research fields and applications, encompassing interfacial catalysis [2–7], bioimaging [8–13], and hyperthermia treatment [14–19]. The excitation of plasmons within these nanoparticles is induced by the interaction between incident light and the free electrons residing in the metal, thereby initiating a collective oscillation of conduction electrons within the NPs [20–24]. This phenomenon leads to a substantial amplification of the electromagnetic field at their surface. This enhanced electromagnetic field plays a pivotal role in governing the observed light absorption properties exhibited by plasmon NPs [25–28].

Furthermore, the integration of plasmon NPs with semiconductors has emerged as a promising avenue for developing Schottky heterojunctions [29–31]. These junctions are formed by combining two different materials, typically a metal and a semiconductor, to create unique electronic and optical properties. By incorporating plasmon NPs into semiconductor materials, the synergies between LSPR of NPs and the properties of semiconductors can be harnessed to enhance the function and performance of heterojunctions in various applications [32,33]. Illuminating these structures with light fields can help overcome the Schottky barrier at the heterojunction interface by promoting hot carrier generation in the LSPR of NPs while enhancing local electromagnetic field strength. This

process can lead to enhanced carrier transfer efficiency and higher carrier concentrations in semiconductors [34,35], thereby improving their overall performance [36]. However, it is important to note that the choice of semiconductor material also plays a pivotal role in determining the extent of this enhancement effect [37]. The selection of a suitable semiconductor material significantly influences both the structural and optical properties of supported plasmon metal NPs. Nevertheless, by manipulating the geometry of these plasmon NPs, it becomes feasible to easily tune the absorption wavelength center of LSPR across a wide range from ultraviolet (UV) [38] to near-infrared (NIR) [39], thus achieving desired absorption characteristics [39–41]. This inherent versatility allows plasmon NPs to enhance nonlinear absorption properties, rendering them highly valuable for light–matter interactions.

In addition, owing to the three-dimensional quantum confinement effects, the III–V InAs/GaAs quantum dot (QD) heterostructure has attracted great interest for a number of applications such as laser diodes, photodetectors, and ultrafast lasers. Among them, the QD-based semiconductor saturable absorption mirror (SESAM) offers many potential advantages such as low saturation fluence, broad laser mode-locked bandwidth, and more flexibility in the laser central operating wavelength over the traditional quantum well-based devices.

In this study, Au NPs were strategically incorporated into III–V semiconductors to form Au/GaAs Schottky heterostructures. The underlying principle behind the LSPR phenomenon of Au NPs was investigated, and the optical absorption enhancement properties of quantum dot semiconductor saturable absorption mirror (QD-SESAM) devices were explored following the integration of plasmon NPs with semiconductor materials. The LSPR effect exhibited by Au NPs in the Au/GaAs Schottky heterojunction significantly amplifies the nonlinearity of QD-SESAM at a near-infrared wavelength of 1550 nm. Consequently, there is an increase in modulation depth (MD) from 2.2% to 2.8% while simultaneously reducing saturation fluence from 16.1 MW/cm<sup>2</sup> to 8.1 MW/cm<sup>2</sup>. Leveraging these enhancements, a Q-switched laser was developed utilizing an enhanced device based on the Au/GaAs Schottky heterojunction as a saturable absorber, resulting in an average output power of 17.61 mW and single pulse energy measuring at 274.9 nJ. This implies that the integration of Au NPs with group III–V semiconductors to establish Schottky heterojunctions represents a highly effective approach for optimizing the optical characteristics of nonlinear devices.

## 2. Experimental Section

### 2.1. QD-SESAM Sample Fabrication

In this study, an InAs/GaAs QD-SESAM was epitaxially grown on an undoped GaAs (100) substrate using molecular beam epitaxy (MBE) equipment. Initially, 31 pairs of quarter-wave Al<sub>0.98</sub>Ga<sub>0.02</sub>As/GaAs were deposited at a growth rate of 1 μm/h and a temperature of 600 °C to form distributed Bragg reflector (DBR) mirrors at the bottom surface of the GaAs substrate. Subsequently, half-wave GaAs and 1 nm In<sub>0.18</sub>Ga<sub>0.82</sub>As buffer layers were grown at 600 °C and 510 °C, respectively. Then, a QD layer consisting of 2.9 ML InAs was developed with a rate of 0.01 ML/s at a temperature of 510 °C while introducing a growth interruption (GI) for durations of 10 s before and after the QD layer growth to achieve more uniform QD formation. Following that, short-period superlattices (SSLs), explicitly consisting of 5 pairs, each comprising In<sub>0.20</sub>Ga<sub>0.80</sub>As (1 nm) and In<sub>0.30</sub>Ga<sub>0.70</sub>As (1 nm), were sequentially deposited during the growth process. The final step involved adding a cap layer by growing a GaAs layer with thicknesses reaching 120 nm on top at 530 °C. Figure 1a illustrates the structural schematic diagram depicting the QD-SESAM configuration. Reflection High-Energy Electron Diffraction (RHEED) is an electron diffraction technique which can yield information on the surface, smoothness, and growth rate of compound semiconductor materials. During the MBE epitaxial growth process, the RHEED graphic analysis system serves as an essential real-time online monitoring tool, enabling the in situ collection of diffraction images to analyze and assess the growth pattern

and quality of the film. Figure 1b,c depict RHEED diffraction images obtained during the DBR growth process of the QD-SESAM for GaAs and  $\text{Al}_{0.98}\text{Ga}_{0.02}\text{As}$ , respectively. In the case of GaAs growth, crystal orientations  $[011]$  and  $[01\bar{1}]$  exhibited  $2\times$  and  $4\times$  patterns, respectively, with a typical  $2\times 4$  reconstruction observed on the sample surface [42]. For  $\text{Al}_{0.98}\text{Ga}_{0.02}\text{As}$  growth, crystal orientations  $[011]$  and  $[01\bar{1}]$  were observed at a frequency of  $2\times$  and  $3\times$  correspondingly with a resulting surface reconstruction of  $2\times 3$  on the sample's surface. Notably, the middle line of the RHEED image appears striped without any discernible broken lines, indicating a highly flat growth surface.

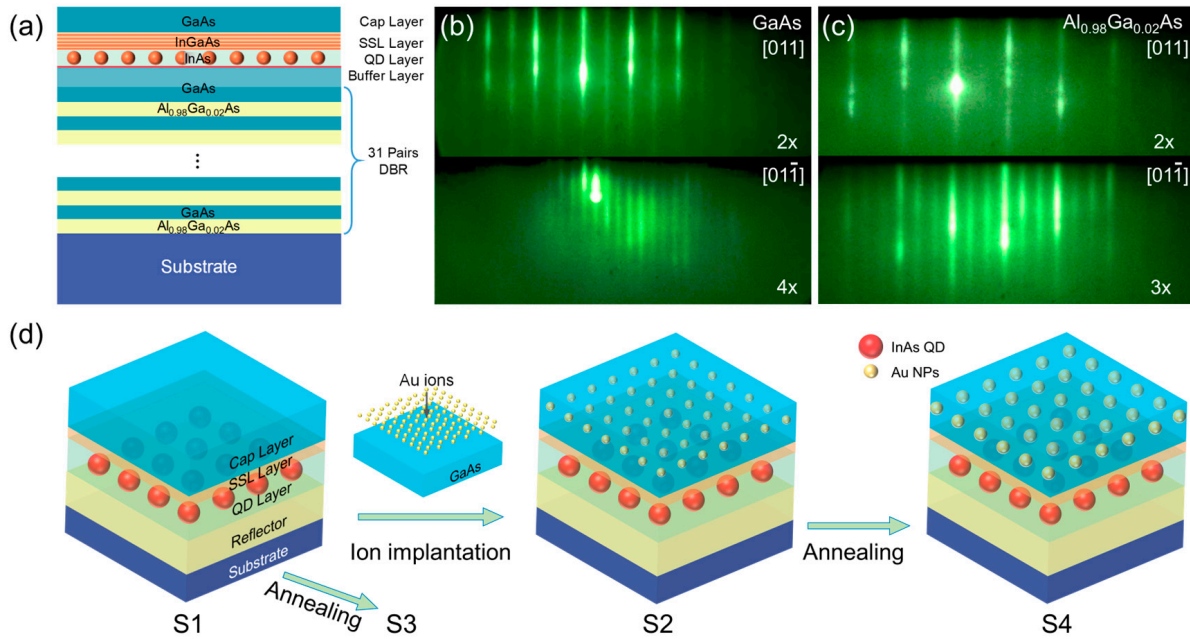


**Figure 1.** (a) Structural schematic diagram of InAs/GaAs QD-SESAM; RHEED images during DBR growth; (b) GaAs; (c)  $\text{Al}_{0.98}\text{Ga}_{0.02}\text{As}$ ; (d) sample fabrication diagram.

The fabrication of Au/GaAs Schottky heterojunction QD-SESAM samples involved the utilization of the ion implantation technique. Specifically, the Au ion implantation process was carried out using the FM2000 metal ion implantation machine. The FM2000 equipment employs an ion beam generated by a Metal Vapor Vacuum Arc (MEVVA) ion source to perform surface modification on the sample material and explore its properties. This procedure involves accelerating high-speed Au ions through an electric field and directing them towards the target material, resulting in collisions with atoms within the target material that lead to energy loss and eventual embedding inside it. When the injection dose surpasses the solid solubility of the substrate, dispersed particles initiate cluster formation, thereby giving rise to metal NPs [43]. The ion implantation method enables the generation of a substrate with a filling factor surpassing the equilibrium solubility threshold for metal NPs implanted in semiconductors, thereby facilitating the formation of metal NPs. The specific manufacturing process is illustrated in Figure 1d. Initially,  $\text{Au}^+$  ion implantation was applied to the GaAs cap layer of the primary QD-SESAM (S1) with an appropriate dose to generate Au NPs, resulting in S2. Subsequently, S1 and S2 were subjected to a heat treatment process in rapid thermal processing (RTP) at a temperature of  $500\text{ }^\circ\text{C}$  for 20 s, with the heating rate set at  $50\text{ }^\circ\text{C/s}$ , resulting in the formation of S3 and S4. Rapid thermal annealing effectively restores the crystal structure, mitigates stress induced by ion implantation [44], and facilitates the nucleation and growth of Au NPs through the swift elevation of sample temperature followed by controlled cooling [45]. Importantly, the annealing temperature remains below that required for QD layer growth, thereby exerting a minimal impact on the QD layer.

## 2.2. Characterization

Scanning electron microscopy (SEM, Apreo S, Thermo Scientific, Waltham, MA, USA) was employed to investigate the cross-sectional structure of the sample. Additionally, atomic force microscopy (AFM, MFP-3D Origin, Oxford Instruments, Abingdon, UK) can offer precise nanoscale measurement outcomes by utilizing the interaction force between the probe and the sample to determine the size, shape, height difference, and surface density of quantum dots on the sample's surface. To further investigate the optical properties of our specimen, we conducted photoluminescence (PL) spectroscopy using our customized equipment. Excitation with a laser wavelength of 532 nm provided ample energy to stimulate electron–hole pairs within the quantum dot system. The resulting emission spectrum exhibited distinct peaks at specific wavelengths indicative of well-defined energy levels within this particular configuration of quantum dots. Moreover, we examined the interaction between light and the sample through reflection absorption spectroscopy, which allowed us to gain valuable insights into its absorption properties by evaluating changes in reflectance and absorbance across a specific range of wavelengths.

## 3. Results and Discussion

Figure 2a illustrates the cross-sectional configuration of S1, showcasing a distinct DBR structure comprising 31 pairs of alternating light and dark stripes. Notably, the bright stripes are GaAs, while the dark stripes are  $\text{Al}_{0.98}\text{Ga}_{0.02}\text{As}$ . The AFM image of the InAs QD layer is presented in Figure 2b, revealing a relatively high point density of approximately  $4.4 \times 10^{10} \text{ cm}^{-2}$  and an observable size distribution among the growing points. Most QDs exhibit an average height of 7.5 nm and an underside width of 40 nm. The PL spectrum of S1 is shown in Figure 2c, revealing two distinct emission peaks at 1351 nm and 1572 nm, which correspond to the SSL and the QD layers, respectively. The reflection absorption spectrum of different QD-SESAM samples is presented in Figure 2d. From the figure, it is evident that all samples exhibit significant light absorption near 1575 nm. Notably, S2 and S4, which incorporate Au/GaAs Schottky heterojunctions, demonstrate enhanced light absorption compared to S1 and S3, suggesting that introducing a Au/GaAs Schottky heterojunction structure promotes light absorption. The overlapping absorption curves of S3 and S1 indicate that the annealing process employed in the experiment has a negligible impact on the QD layer. The decrease in maximum reflectance observed for S2 can be attributed to stress induced by Au ion implantation. However, after annealing treatment, the maximum reflectance of S4 recovers significantly, indicating the effective relief from implantation-induced stress. Furthermore, owing to its superior light absorption characteristics relative to S2, it is apparent that S4 possesses more significant potential as a saturable absorber (SA).

Figure 3a illustrates a schematic diagram of the carrier transfer mechanism in the absorption region of the Au/GaAs Schottky heterojunction sample, aiming to elucidate the impact of Au NPs and the Au/GaAs Schottky heterojunction on carrier migration and transfer within the sample. The distinctive optical and electronic properties of Au NPs have been extensively documented [22,46,47]. In the realm of nonlinear optics, the incorporation of Au NPs with low-dimensional material systems also enables the manipulation of third-order nonlinear optical properties in devices through birefringence and two-photon absorption effects, thereby exerting a profound influence on their performance [48]. Upon embedding a Au nanoparticle onto the device surface, it scatters incident light and locally amplifies the electromagnetic field. Consequently, this leads to an enhancement in both the effective absorption cross-section and effective optical path length inside the semiconductor. Due to the presence of Au nanoparticles, when light interacts with the device's surface, a fraction of it scatters and alters its propagation direction. This scattering phenomenon facilitates increased interaction between light and the material, thereby enhancing the device's absorption capacity towards incident light. Furthermore, the electromagnetic field generated around the Au NPs further amplifies the material's light absorption. As depicted in Figure 3a, the interaction between incident light and Au NPs induces the

localized surface plasmon resonance (LSPR) effect, resulting in an electromagnetic field that promotes carrier transfer and augments light absorption within the sample through two distinct mechanisms [46,49]. (i) Robust interactions between light and free electrons in Au NPs generate hot charge carriers (electrons) capable of traversing the Schottky barrier of Au/GaAs Schottky heterojunctions, with excited hot electrons being directly transferred to neighboring GaAs (direct electron transfer, DET). (ii) The enhancement of the local electromagnetic field (LEMF) occurs near the Au/GaAs Schottky heterojunction interface when interacting with incident light, leading to the localized generation of electron–hole pairs in GaAs and the amplification of local carrier density. The carriers in GaAs undergo migration towards InAs QDs through the SSL structure, where they are effectively captured and emit light at a wavelength of 1572 nm. During the carrier’s passage through the SSL barrier, it experiences scattering by superlattice phonons, leading to the significantly enhanced relaxation of carrier energy and improved trapping efficiency within the QDs [50]. Simultaneously, carriers recombine within the SSL structure, resulting in a light emission of 1351 nm. When working, when the light pulse passes through the InAs QDs, its central part exhibits higher intensity and transmittance, while the flanking part exhibits lower intensity and transmittance. This difference causes the edge loss of the light pulse to be larger than the center part, which narrows the light pulse and produces a narrow pulse output after many cycles in the resonator.

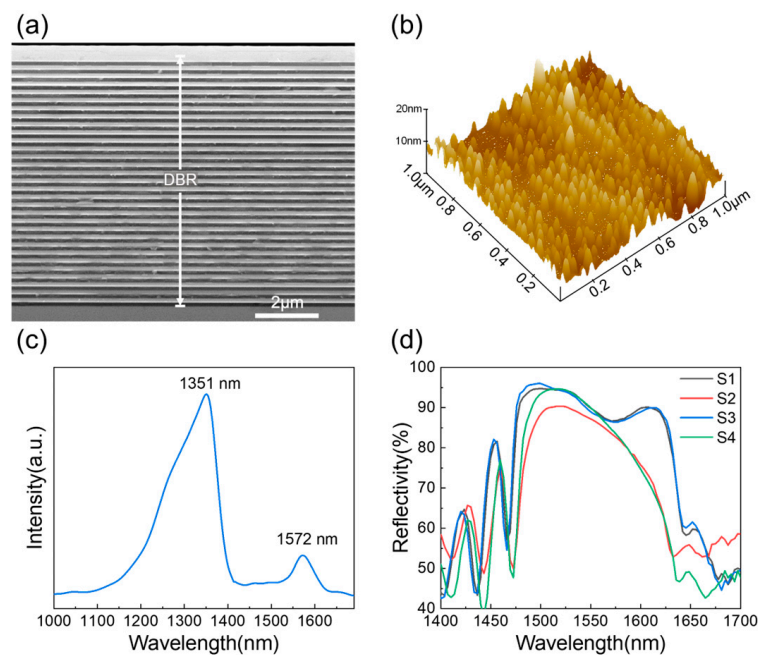


**Figure 2.** (a) SEM image of cross-section S1; (b) a  $1 \times 1 \mu\text{m}^2$  AFM image of InAs/GaAs QDs grown without capping layer; (c) PL spectrum of S1; (d) reflectance absorption spectrum of samples.

To achieve a robust enhancement of LSPR, the Au ion implantation was carried out at an energy of 140 keV and a dose of  $5.0 \times 10^{16}$  ions/cm<sup>2</sup>, as calculated using the Stopping and Range of Ions in Matter (SRIM) program. Figure 3b illustrates the distribution of ions post-implantation, which exhibits a nearly Gaussian profile within the depth range of 0–60 nm, with its peak at 26 nm. The LEMF enhancement distribution at the Au/GaAs Schottky heterojunction interface with varying diameters of Au NPs was simulated by Finite-Difference Time-Domain (FDTD). As depicted in Figure 3c, the  $E_{\text{max}}$  field intensity exhibits an evident increase as the diameter of Au NPs increases. This implies that the annealing process enhances both the nucleation and growth effects on Au NPs, thereby amplifying the LEMF and optimizing device performance. Figure 3d,e depict the near-field distribution of Au NPs with sizes of 6 nm and 20 nm, respectively. Notably, a

significant enhancement in LEMF is observed at the heterojunction interface, with a larger enhancement range and intensity observed for the 20 nm Au NPs.

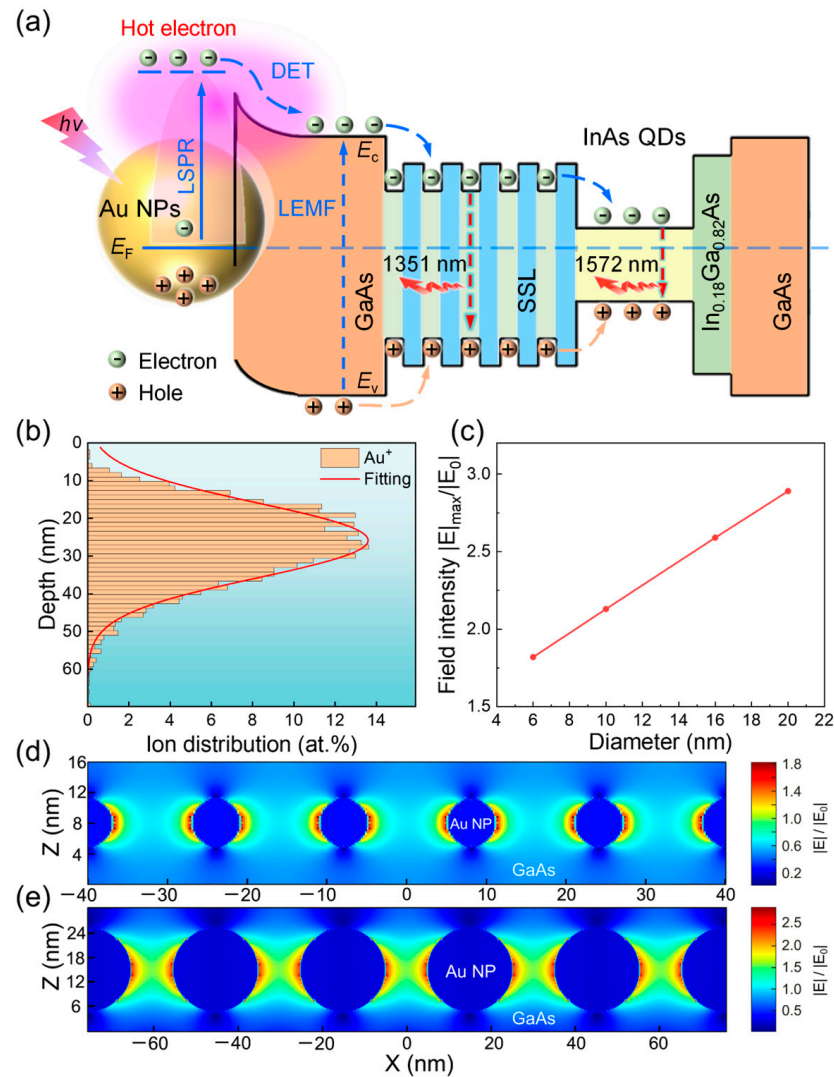


**Figure 3.** (a) Schematic representation of the transfer mechanism of photogenerated carriers in Au/GaAs Schottky heterojunction samples; (b) SRIM simulation results of Au ion distribution; (c) variation in  $E_{\max}$  field intensity for different Au NP diameters simulated by FDTD; FDTD simulation of 6 nm (d) and 20 nm (e) diameter Au NPs with near-field distributions.

To explore the nonlinear optical absorption of QD-SESAM, we have established a measurement system for nonlinear saturable absorption featuring double-balanced detectors. As depicted in Figure 4a, a self-constructed mode-locked fiber laser operating at a central wavelength of 1561 nm, pulse width of 870 fs, and repetition rate of 13.4 MHz was employed as the seed light source. Following amplification by an erbium-doped fiber amplifier (EDFA), the laser beam is split into two equal-intensity beams using a 50/50 optical coupler (OC). One beam is directed towards the power meter (PM1) via saturable absorber mirror (SAM) incorporated within a circulator (CIR), while the other beam is directly transmitted to the power meter (PM2). The nonlinear optical absorption curves of the S1, S2, S3, and S4 QD-SESAMs are presented in Figure 4b–e. The curve fitting was performed using the following formula [51]:

$$R = 1 - \Delta R \times \exp(-F/F_{sat}) - R_{ns} \quad (1)$$

where  $R$  is the reflectivity,  $\Delta R$  is the MD,  $F$  is the input fluence,  $F_{sat}$  is the saturation fluence, and  $R_{ns}$  refers to the non-saturable losses.

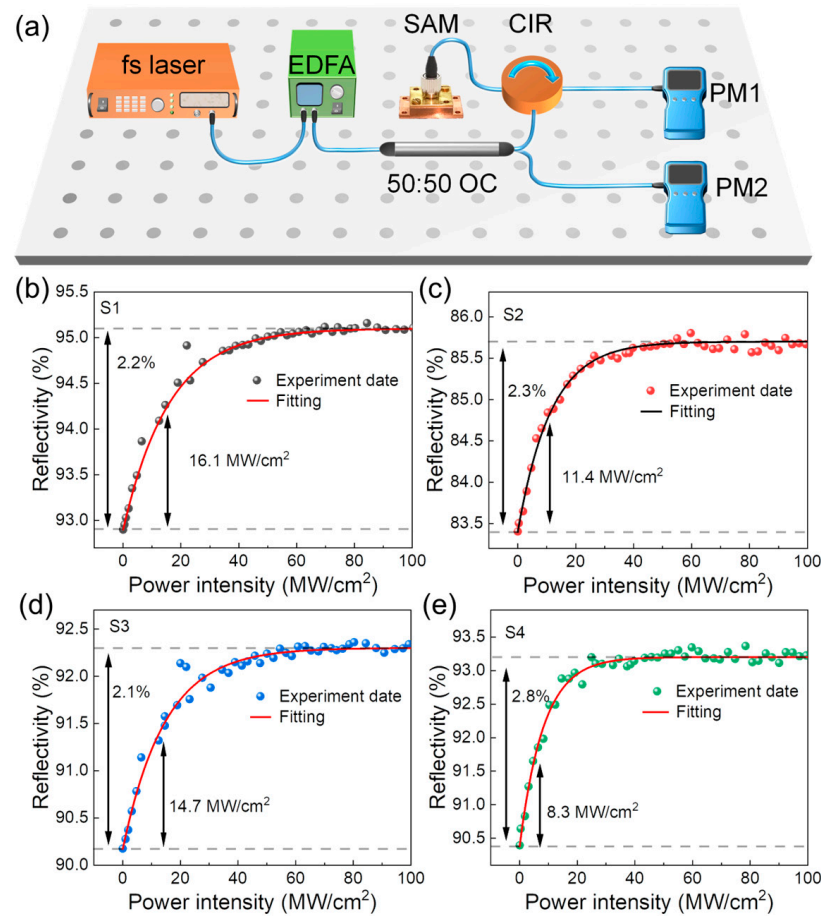


**Figure 4.** (a) Schematic representation of a device for measuring nonlinear optical absorption; nonlinear reflection and fitting curves of S1 (b), S2 (c), S3 (d), and S4 (e).

As depicted in Figure 4b–e, the original QD-SESAM (S1) exhibits a modest MD of only 2.2% and an  $F_{sat}$  value of 16.1 MW/cm<sup>2</sup>. Following Au ion implantation, the  $F_{sat}$  of S2 experiences a significant reduction to 11.4 MW/cm<sup>2</sup>, indicating that a Au/GaAs Schottky heterojunction after implantation remarkably enhances optical absorption within the sample by facilitating carrier transfer. The only marginal enhancement of the MD in S2 is due to the incomplete release of stress caused by Au ion implantation. The  $F_{sat}$  for S3 slightly decreased to 14.7 MW/cm<sup>2</sup> owing to the elimination of non-radiative recombination centers in the sample through annealing. Following annealing with S2, the S4 sample demonstrated a significant enhancement in MD to 2.8%, while  $F_{sat}$  was reduced to 8.3 MW/cm<sup>2</sup>, indicating that annealing effectively released the stress induced by the Au ion implantation process. Simultaneously, annealing induced the nucleation and growth of Au NPs, thereby reinforcing the LSPR effect of the Au/GaAs Schottky heterojunction and significantly optimizing the nonlinear optical properties of the device.

As depicted in Figure 5, we constructed a polarization-maintaining erbium-doped fiber (EDF) ring cavity laser system to investigate the Q-switching characteristics of S4 as the SAM. The laser system is powered by a 976 nm laser diode (LD) as the pump source, which is connected to a wavelength division multiplexer (WDM), a 1.1 m EDF, a polarization-independent isolator (PI-ISO), a CIR, and an OC via a polarization-maintaining fiber (PMF) to establish a ring cavity configuration. The light confined within the cavity is directed towards the SAM through the CIR for generating Q-switched pulses, ultimately resulting in an output of the laser with 10% intensity through the OC for subsequent analysis

purposes. The illustration shows the image of the S4 and the measurement system for the real-time monitoring of the output characteristics of the Q-switched laser. The measurement system comprises a digital storage high-speed oscilloscope (Keysight DSOS054A), optical spectrum analyzer (Anritsu MS9740A), radio frequency (RF) spectrum analyzer (Keysight N9322C), and digital display power meter. These instruments are employed to monitor and record the temporal, optical spectrum, RF spectrum, and power characteristics of laser pulses correspondingly.

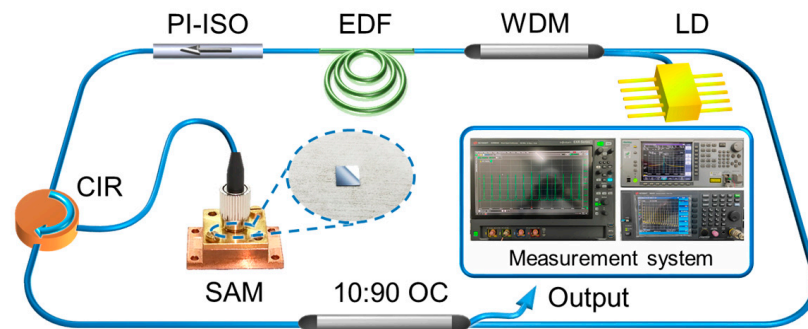


**Figure 5.** Schematic diagram of Er-doped fiber ring laser. The illustrations show images of the sample and the measurement system used to monitor the output characteristics correspondingly.

The passive Q-switching technique, utilizing S4 as SAM, primarily relies on its saturable absorption characteristics to periodically regulate the resonator's loss for achieving pulsed light output. Initially, the cavity exhibits feeble light gain with a significantly high absorption coefficient and low transmittance of the SA, resulting in a state of elevated loss where laser oscillation cannot be established. As the pump power intensifies, an accumulation of inverted particles occurs, leading to enhanced optical gain within the cavity. Once the pump surpasses the loss and achieves a higher gain, pulse generation initiates gradually. The power within the resonator then steadily rises from spontaneous radiation noise until it reaches sufficient intensity for SA saturation. Subsequently, as the S4 becomes fully saturated, there is an accelerated increase in power until reaching maximum pulse power when the net gain equals to zero. As the gain further depletes, it transitions into negative net gain territory causing a gradual decay in resonator power. After the emission of the pulse, there is a decrease in light intensity within the resonant cavity and the absorber reverts back to a state of high loss before the gain recovers. Consequently, this delay causes the subsequent pulse to be postponed until the complete replenishment of energy occurs within the gain medium.

The S4 was inserted into the designed ring cavity as SAM, and the pump power gradually increased to 33.83 mW, corresponding to the continuous Q-switching mode. As the pump power increases, both pulse intensity and repetition frequency gradually increase. Figure 6a illustrates the evolution of the Q-switched pulse train at different pump powers. Obviously, the output pulse sequence remains stable and relatively uniform during adjustments in pump power, with a reasonable intensity distribution. These observations indicate that the fiber laser operates in a highly stable Q-switching state. The corresponding pulse sequences, RF spectrum, and optical spectrum at a pump power of 649 mW are illustrated in Figure 6b–d. As depicted in Figure 6b, the Q-switched pulse sequence exhibits remarkable regularity with a stable intensity and a Gaussian-like distribution of the pulse shape having a width of 1.97  $\mu\text{s}$ . The observed fixed time interval between pulses is measured to be 19.72  $\mu\text{s}$ , which aligns well with the findings obtained from RF spectrum analysis (Figure 6c), indicating a pulse repetition rate of 50.71 kHz. Moreover, Figure 6c shows that the signal-to-noise ratio (SNR) of the fundamental frequency reaches up to an impressive value of 60 dB, implying the steady operation of the laser system while the central wavelength for the laser pulse is found to be at around 1561.2 nm as shown in Figure 6d.

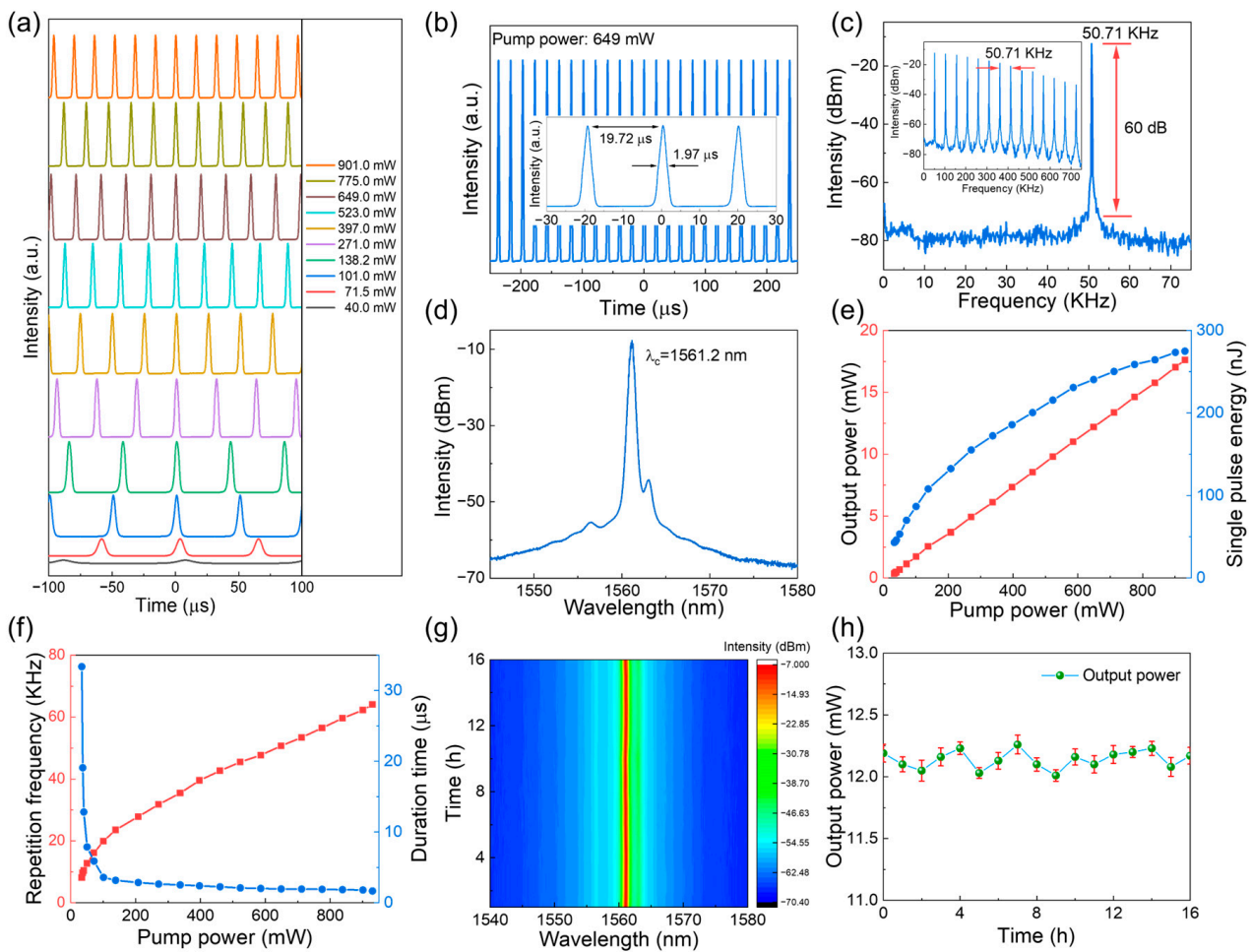


**Figure 6.** Output characteristics of Q-switched EDF laser based on S4: (a) pulse train evolution under different pump power; the pulse train (b), RF spectrum (c), and optical spectrum (d) at the pump power of 649 mW; (e) evolution curve of output power and single pulse energy with pump power; (f) pump power-dependent repetition frequency and pulse duration; the stability of output characteristics (g) and output power (h) over time.

Figure 6e illustrates the power output of the Q-switched laser and its correlation with single pulse energy as a function of pump power. With an increase in pump power from 33.83 mW to 930.6 mW, there was a corresponding rise in output power from 0.35 mW to 17.61 mW, accompanied by an escalation in single pulse energy from 43.05 nJ to 274.9 nJ. Figure 6f demonstrates the relationship between pulse repetition rate, duration time, and pump power, revealing that as the latter increases, the former escalates from 8.13 kHz to 64.06 kHz while concurrently witnessing a decrease in pulse duration time from 33.38 μs to 1.68 μs. To assess the long-term operational stability of the Q-switched laser, we conducted a series of measurements over a 16 h period at an interval of 1 h, while maintaining a pump power of 649 mW. The recorded optical spectrum and output power are presented in Figure 6g and h, respectively. The error bar in Figure 6h represents the standard deviation of the power data. Notably, no significant drift was observed in the central wavelength of the laser output, indicating its remarkable stability. Additionally, there were no noticeable fluctuations in spectral intensity throughout the measurement duration. Moreover, it is worth mentioning that the output power remained consistently stable at approximately 12.1 mW. These findings underscore the exceptional reliability and stability exhibited by our Q-switched laser system, further highlighting its commendable long-term output capability.

#### 4. Conclusions

In this study, Au NPs were strategically incorporated into III-V semiconductors to form Au/GaAs Schottky heterostructures. The stress induced by the injection was effectively alleviated through rapid thermal annealing. The carrier-enhancing effect of the unique LSPR effect of Au NPs at the heterojunction interface was demonstrated by analyzing the Au/GaAs Schottky heterojunction. The MD of the optimized QD-SESAM was significantly improved from 2.2% to 2.8%, and the saturation fluence was significantly reduced from 16.1 MW/cm<sup>2</sup> to 8.3 MW/cm<sup>2</sup>. A Q-switched laser was constructed based on the optimized sample (S4) as a SAM, with an average output power of 17.61 mW and a single pulse energy of 274.9 nJ. The present study showcases the carrier enhancement effect of Au/GaAs Schottky heterojunctions, substantiating the utilization of a Au NP-based LSPR effect in the capping technique of Au/GaAs heterojunction devices to enhance their nonlinear characteristics. This demonstration highlights its unique superiority and paves a novel pathway for tailoring the nonlinear absorption properties of III-V SESAMs by incorporating Au NPs.

**Author Contributions:** Conceptualization, C.J. and Z.Z.; Data curation, H.W., C.J. and Z.Z.; Formal analysis, H.D. and Z.Z.; Funding acquisition, C.J.; Methodology, H.W.; Project administration, S.L.; Software, H.W., H.D. and M.L.; Supervision, S.L. and Z.Z.; Writing—original draft, H.W. and Z.Z.; Writing—review and editing, H.W., C.J., S.L. and Z.Z. All authors have read and agreed to the published version of the manuscript.

**Funding:** This research was funded by the Youth Foundation of Shandong Natural Science Foundation of China, grant number ZR2023QE216.

**Institutional Review Board Statement:** Not applicable.

**Informed Consent Statement:** Not applicable.

**Data Availability Statement:** The data presented in this study are available on request from the corresponding author.

**Conflicts of Interest:** The authors declare no conflicts of interest.

#### References

1. Han, X.; Tian, J.; Li, Z.; Wu, T.; Ji, G.; Li, S.; Xing, F.; Zhang, Y. Broadband refractive index sensor based on localized surface plasmon for highly sensitive detection of fluid pressure. *Appl. Surf. Sci.* **2022**, *587*, 152873. [[CrossRef](#)]
2. Xu, G.; Du, X.; Wang, W.; Qu, Y.; Liu, X.; Zhao, M.; Li, W.; Li, Y.Q. Plasmonic Nanozymes: Leveraging Localized Surface Plasmon Resonance to Boost the Enzyme-Mimicking Activity of Nanomaterials. *Small* **2022**, *18*, 2204131. [[CrossRef](#)]
3. Araujo, T.P.; Quiroz, J.; Barbosa, E.C.M.; Camargo, P.H.C. Understanding plasmonic catalysis with controlled nanomaterials based on catalytic and plasmonic metals. *Curr. Opin. Colloid Interface Sci.* **2019**, *39*, 110–122. [[CrossRef](#)]
4. Feng, Y.; Dechezelles, J.-F.; D’Acremont, Q.; Courtade, E.; De Waele, V.; Pera-Titus, M.; Nardello-Rataj, V. Light-driven Pickering interfacial catalysis for the oxidation of alkenes at near-room temperature. *Green Chem.* **2023**, *25*, 1417–1423. [[CrossRef](#)]
5. Rodrigues, M.P.d.S.; Dourado, A.H.B.; Cutolo, L.d.O.; Parreira, L.S.; Alves, T.V.; Slater, T.J.A.; Haigh, S.J.; Camargo, P.H.C.; Cordoba de Torresi, S.I. Gold–Rhodium Nanoflowers for the Plasmon-Enhanced Hydrogen Evolution Reaction under Visible Light. *ACS Catal.* **2021**, *11*, 13543–13555. [[CrossRef](#)]
6. Zhao, J.; Xue, S.; Ji, R.; Li, B.; Li, J. Localized surface plasmon resonance for enhanced electrocatalysis. *Chem. Soc. Rev.* **2021**, *50*, 12070–12097. [[CrossRef](#)] [[PubMed](#)]
7. Wang, M.; Tang, Y.; Jin, Y. Modulating Catalytic Performance of Metal–Organic Framework Composites by Localized Surface Plasmon Resonance. *ACS Catal.* **2019**, *9*, 11502–11514. [[CrossRef](#)]
8. Luo, X.; Liu, J. Ultrasmall Luminescent Metal Nanoparticles: Surface Engineering Strategies for Biological Targeting and Imaging. *Adv. Sci.* **2021**, *9*, 2103971. [[CrossRef](#)] [[PubMed](#)]
9. Lenzi, E.; Jimenez de Aberasturi, D.; Liz-Marzán, L.M. Surface-Enhanced Raman Scattering Tags for Three-Dimensional Bioimaging and Biomarker Detection. *ACS Sens.* **2019**, *4*, 1126–1137. [[CrossRef](#)] [[PubMed](#)]
10. Si, P.; Razmi, N.; Nur, O.; Solanki, S.; Pandey, C.M.; Gupta, R.K.; Malhotra, B.D.; Willander, M.; de la Zerda, A. Gold nanomaterials for optical biosensing and bioimaging. *Nanoscale Adv.* **2021**, *3*, 2679–2698. [[CrossRef](#)] [[PubMed](#)]
11. Ou, X.; Liu, Y.; Zhang, M.; Hua, L.; Zhan, S. Plasmonic gold nanostructures for biosensing and bioimaging. *Microchim. Acta* **2021**, *188*, 304. [[CrossRef](#)]
12. Tan, P.; Li, H.; Wang, J.; Gopinath, S.C.B. Silver nanoparticle in biosensor and bioimaging: Clinical perspectives. *Biotechnol. Appl. Biochem.* **2021**, *68*, 1236–1242. [[CrossRef](#)]

13. Ma, J.; Wang, X.; Feng, J.; Huang, C.; Fan, Z. Individual Plasmonic Nanoprobes for Biosensing and Bioimaging: Recent Advances and Perspectives. *Small* **2021**, *17*, 2004287. [[CrossRef](#)]
14. de la Encarnación, C.; Jimenez de Aberasturi, D.; Liz-Marzán, L.M. Multifunctional plasmonic-magnetic nanoparticles for bioimaging and hyperthermia. *Adv. Drug Deliv. Rev.* **2022**, *189*, 114484. [[CrossRef](#)]
15. Yang, M.-C.; Hardiansyah, A.; Cheng, Y.-W.; Liao, H.-L.; Wang, K.-S.; Randy, A.; Harito, C.; Chen, J.-S.; Jeng, R.-J.; Liu, T.-Y. Reduced graphene oxide nanosheets decorated with core-shell of Fe<sub>3</sub>O<sub>4</sub>-Au nanoparticles for rapid SERS detection and hyperthermia treatment of bacteria. *Spectrochim. Acta Part A Mol. Biomol. Spectrosc.* **2022**, *281*, 121578. [[CrossRef](#)] [[PubMed](#)]
16. He, Y.; Yang, M.; Zhao, S.; Cong, C.; Li, X.; Cheng, X.; Yang, J.; Gao, D. Regulatory Mechanism of Localized Surface Plasmon Resonance Based on Gold Nanoparticles-Coated Paclitaxel Nanoliposomes and Their Antitumor Efficacy. *ACS Sustain. Chem. Eng.* **2018**, *6*, 13543–13550. [[CrossRef](#)]
17. Garcés, V.; González, A.; Gálvez, N.; Delgado-López, J.M.; Calvino, J.J.; Trasobares, S.; Fernández-Afonso, Y.; Gutiérrez, L.; Dominguez-Vera, J.M. Magneto-optical hyperthermia agents based on probiotic bacteria loaded with magnetic and gold nanoparticles. *Nanoscale* **2022**, *14*, 5716–5724. [[CrossRef](#)] [[PubMed](#)]
18. Rommelfanger, N.J.; Ou, Z.; Keck, C.H.C.; Hong, G. Differential Heating of Metal Nanostructures at Radio Frequencies. *Phys. Rev. Appl.* **2021**, *15*, 054007. [[CrossRef](#)] [[PubMed](#)]
19. Maamoun, W.; Badawi, M.I.; Aly, A.A.; Khedr, Y. Nanoparticles in enhancing microwave imaging and microwave Hyperthermia effect for liver cancer treatment. *Rev. Adv. Mater. Sci.* **2021**, *60*, 223–236. [[CrossRef](#)]
20. Alharbi, R.; Irannejad, M.; Yavuz, M. A Short Review on the Role of the Metal-Graphene Hybrid Nanostructure in Promoting the Localized Surface Plasmon Resonance Sensor Performance. *Sensors* **2019**, *19*, 862. [[CrossRef](#)]
21. Wang, L.; Hasanzadeh Kafshgari, M.; Meunier, M. Optical Properties and Applications of Plasmonic-Metal Nanoparticles. *Adv. Funct. Mater.* **2020**, *30*, 2005400. [[CrossRef](#)]
22. Li, R.; Pang, C.; Li, Z.; Yang, M.; Amekura, H.; Dong, N.; Wang, J.; Ren, F.; Wu, Q.; Chen, F. Fused Silica with Embedded 2D-Like Ag Nanoparticle Monolayer: Tunable Saturable Absorbers by Interparticle Spacing Manipulation. *Laser Photonics Rev.* **2020**, *14*, 1900302. [[CrossRef](#)]
23. Pang, C.; Li, R.; Li, Z.; Dong, N.; Cheng, C.; Nie, W.; Böttger, R.; Zhou, S.; Wang, J.; Chen, F. Lithium Niobate Crystal with Embedded Au Nanoparticles: A New Saturable Absorber for Efficient Mode-Locking of Ultrafast Laser Pulses at 1  $\mu\text{m}$ . *Adv. Opt. Mater.* **2018**, *6*, 1800357. [[CrossRef](#)]
24. Sun, X.; Ye, Q.; Liu, Y.; Sun, W.; Pang, C.; Jia, Y.; Chen, F. Plasmon-enhanced Raman scattering of 2D materials via embedded silver nanoparticles in glass. *J. Appl. Phys.* **2023**, *133*, 084304. [[CrossRef](#)]
25. Sun, X.; Jia, Y.; Nie, H.; Ren, F.; Zhang, B.; Chen, F. Near-Surface Buried Plasmonic Nanoparticles in Glass as Novel Nonlinear Saturable Absorbers for Ultrafast Lasers. *Adv. Opt. Mater.* **2021**, *10*, 2101664. [[CrossRef](#)]
26. Dai, H.; Wang, H.; Chu, H.; Huang, Y.; Wei, C.; Zhang, Z.; Jiang, C. Cascade amplification of optical absorption on III–V semiconductors via plasmon-coupled graphene. *Appl. Phys. Lett.* **2023**, *123*, 221101. [[CrossRef](#)]
27. Mohammadi, M.h.; Eskandari, M.; Fathi, D. Effects of the location and size of plasmonic nanoparticles (Ag and Au) in improving the optical absorption and efficiency of perovskite solar cells. *J. Alloys Compd.* **2021**, *877*, 160177. [[CrossRef](#)]
28. Gong, H.; Cui, Z.; Shao, W.; Ma, X. Investigation of a novel surface inlay composite nanoparticle based on local surface plasmon resonance-enhanced solar absorption. *Renew. Energy* **2022**, *197*, 452–461. [[CrossRef](#)]
29. Shao, Z.; Jia, H.; Zhang, Y.; Yang, X.; Zhong, M.; Chang, C. Oxygen Vacancy-Mediated Interfacial Charge Transfer of Au/ZnO Schottky Heterojunctions for Enhanced UV Photodegradation. *Int. J. Photoenergy* **2020**, *2020*, 2456968. [[CrossRef](#)]
30. Qiu, C.; Zhang, H.; Tian, C.; Jin, X.; Song, Q.; Xu, L.; Ijaz, M.; Blaikie, R.J.; Xu, Q. Breaking bandgap limitation: Improved photosensitization in plasmonic-based CsPbBr<sub>3</sub> photodetectors via hot-electron injection. *Appl. Phys. Lett.* **2023**, *122*, 243502. [[CrossRef](#)]
31. Yuan, C.; Yin, H.; Lv, H.; Zhang, Y.; Li, J.; Xiao, D.; Yang, X.; Zhang, Y.; Zhang, P. Defect and Donor Manipulated Highly Efficient Electron–Hole Separation in a 3D Nanoporous Schottky Heterojunction. *JACS Au* **2023**, *3*, 3127–3140. [[CrossRef](#)]
32. Song, J.; Long, J.; Liu, Y.; Xu, Z.; Ge, A.; Piercy, B.D.; Cullen, D.A.; Ivanov, I.N.; McBride, J.R.; Losego, M.D.; et al. Highly Efficient Plasmon Induced Hot-Electron Transfer at Ag/TiO<sub>2</sub> Interface. *ACS Photonics* **2021**, *8*, 1497–1504. [[CrossRef](#)]
33. Yu, Y.; Sun, Y.; Hu, Z.; An, X.; Zhou, D.; Zhou, H.; Wang, W.; Liu, K.; Jiang, J.; Yang, D.; et al. Fast Photoelectric Conversion in the Near-Infrared Enabled by Plasmon-Induced Hot-Electron Transfer. *Adv. Mater.* **2019**, *31*, 1903829. [[CrossRef](#)]
34. Kumar, A.; Ahuja, J.; Mondal, A.; Bag, A. Ga-In Nanoparticle Induced UV Plasmonic Impact on Heterojunction Based Deep UV Photodetector. *IEEE Trans. Nanotechnol.* **2022**, *21*, 196–203. [[CrossRef](#)]
35. Khan, M.R.; Chuan, T.W.; Yousuf, A.; Chowdhury, M.N.K.; Cheng, C.K. Schottky barrier and surface plasmonic resonance phenomena towards the photocatalytic reaction: Study of their mechanisms to enhance photocatalytic activity. *Catal. Sci. Technol.* **2015**, *5*, 2522–2531. [[CrossRef](#)]
36. Li, Z.; Wang, Z.; Li, J.; Zhu, Q.; Wang, Z.; Dai, Z. Enhancing Photoelectric Response of an Au@Ag/AgI Schottky Contact through Regulation of Localized Surface Plasmon Resonance. *J. Am. Chem. Soc.* **2021**, *143*, 13478–13482. [[CrossRef](#)]
37. Di Bartolomeo, A. Graphene Schottky diodes: An experimental review of the rectifying graphene/semiconductor heterojunction. *Phys. Rep.* **2016**, *606*, 1–58. [[CrossRef](#)]
38. Huang, J.; Li, Q.; Lu, X.; Meng, J.; Li, Z. LSPR-Enhanced Pyro-Phototronic Effect for UV Detection with an Ag–ZnO Schottky Junction Device. *Adv. Mater. Interfaces* **2022**, *9*, 2200327. [[CrossRef](#)]

39. Xu, Y.; Qiu, P.; Mao, J.; Jile, H.; Jiang, P. Dual-band narrow-band absorber with perfect absorption peaks in mid-infrared and near-infrared based on surface plasmon resonance. *Diam. Relat. Mater.* **2023**, *132*, 109624. [[CrossRef](#)]
40. Patra, N.; Manikandan, M.; Singh, V.; Palani, I.A. Investigations on LSPR effect of Cu/Al nanostructures on ZnO nanorods towards photodetector applications. *J. Lumin.* **2021**, *238*, 118331. [[CrossRef](#)]
41. Gao, Y.; Murai, S.; Shinozaki, K.; Ishii, S.; Tanaka, K. Aluminum for Near Infrared Plasmonics: Amplified Up-Conversion Photoluminescence from Core-Shell Nanoparticles on Periodic Lattices. *Adv. Opt. Mater.* **2021**, *9*, 2001040. [[CrossRef](#)]
42. Hong, M.; Kwo, J.; Kortan, A.R.; Mannaerts, J.P.; Sergent, A.M. Epitaxial Cubic Gadolinium Oxide as a Dielectric for Gallium Arsenide Passivation. *Science* **1999**, *283*, 1897–1900. [[CrossRef](#)]
43. Chu, H.; Wang, H.; Huang, Y.; Dai, H.; Lv, M.; Zhang, Z.; Jiang, C. Investigation of the Optical Nonlinearity for Au Plasmonic Nanoparticles Based on Ion Implantation. *Nanomaterials* **2023**, *13*, 2662. [[CrossRef](#)] [[PubMed](#)]
44. Parker, J.S.; Sivananthan, A.; Norberg, E.; Coldren, L.A. Regrowth-free high-gain InGaAsP/InP active-passive platform via ion implantation. *Opt. Express* **2012**, *20*, 19946–19955. [[CrossRef](#)] [[PubMed](#)]
45. Ramaswamy, V.; Haynes, T.E.; White, C.W.; MoberlyChan, W.J.; Roorda, S.; Aziz, M.J. Synthesis of Nearly Monodisperse Embedded Nanoparticles by Separating Nucleation and Growth in Ion Implantation. *Nano Lett.* **2005**, *5*, 373–377. [[CrossRef](#)]
46. Wang, C.; Zhang, H.; Lai, F.; Xie, Z.; Hau Ng, Y.; Weng, B.; Wu, X.; Liao, Y. Engineering versatile Au-based catalysts for solar-to-fuel conversion. *J. Energy Chem.* **2023**, *83*, 341–362. [[CrossRef](#)]
47. Yao, J.; Jiang, Y.; Gu, X.; Guo, X.; Ying, Y.; Wen, Y.; Liu, X.; Yang, H.; Wu, Y. Surface Plasmon Resonance-Triggered Local Electromagnetic Field Advances Photocatalytic and Photoelectrochemical Performance of Plasmonic Metal/Semiconductor Composite. *J. Phys. Chem. C* **2022**, *127*, 248–255. [[CrossRef](#)]
48. Carrillo-Delgado, C.; Torres-Torres, D.; Trejo-Valdez, M.; Rebollo, N.R.; Hernández-Gómez, L.H.; Torres-Torres, C. Bidirectional optical Kerr transmittance in a bilayer nanocomposite with Au nanoparticles and carbon nanotubes. *Phys. Scr.* **2015**, *90*, 085804. [[CrossRef](#)]
49. Cushing, S.K.; Li, J.; Meng, F.; Senty, T.R.; Suri, S.; Zhi, M.; Li, M.; Bristow, A.D.; Wu, N. Photocatalytic Activity Enhanced by Plasmonic Resonant Energy Transfer from Metal to Semiconductor. *J. Am. Chem. Soc.* **2012**, *134*, 15033–15041. [[CrossRef](#)]
50. Jiang, C.; Ning, J.; Li, X.; Wang, X.; Zhang, Z. Development of a 1550-nm InAs/GaAs Quantum Dot Saturable Absorber Mirror with a Short-Period Superlattice Capping Structure towards Femtosecond Fiber Laser Applications. *Nanoscale Res. Lett.* **2019**, *14*, 362. [[CrossRef](#)]
51. Finke, T.; Nurnberg, J.; Sichkovskiy, V.; Golling, M.; Keller, U.; Reithmaier, J.P. Temperature resistant fast In<sub>x</sub>Ga<sub>1-x</sub>As / GaAs quantum dot saturable absorber for the epitaxial integration into semiconductor surface emitting lasers. *Opt. Express* **2020**, *28*, 20954–20966. [[CrossRef](#)] [[PubMed](#)]

**Disclaimer/Publisher's Note:** The statements, opinions and data contained in all publications are solely those of the individual author(s) and contributor(s) and not of MDPI and/or the editor(s). MDPI and/or the editor(s) disclaim responsibility for any injury to people or property resulting from any ideas, methods, instructions or products referred to in the content.